Correction for Geometric Distortion in Echo Planar Images from B_0 Field Variations

Peter Jezzard, Robert S. Balaban

A method is described for the correction of geometric distortions occurring in echo planar images. The geometric distortions are caused in large part by static magnetic field inhomogeneities, leading to pixel shifts, particularly in the phase encode direction. By characterizing the field inhomogeneities from a field map, the image can be unwarped so that accurate alignment to conventionally collected images can be made. The algorithm to perform the unwarping is described, and results from echo planar images collected at 1.5 and 4 Tesla are shown.

Key words: echo planar imaging, EPI; geometric distortion; field map correction.

INTRODUCTION

Echo planar imaging (EPI) was conceived and developed by Mansfield's group in Nottingham (1, 2) and further developed by others (3). Initially a little used sequence, mainly due to its strenuous hardware demands, EPI is becoming increasingly popular as a rapid method of collecting low to medium resolution images, and is finding much use in the characterization of dynamic time series, such as tracking a bolus injection of contrast agent through the brain (4) to measure regional cerebral blood volume, or dynamic time series imaging of blood oxygenation level dependent contrast (5, 6).

Many of these applications require accurate registration between the (often) low resolution echo planar images (of 64 × 64 or 128 × 128 pixels) that may reflect some sort of functional detail, and high resolution conventionally collected images that exhibit good anatomical detail. A major problem in achieving this goal is the inevitable geometric distortion that accompanies EPI data sets, making such co-registration difficult or impossible. The main cause of geometric distortion in echo planar images is the residual magnetic field inhomogeneity, due both to the external room temperature shim coils not being optimally set, and also to high order internal magnetic field inhomogeneities in the sample, which cannot always easily be shimmed out using external coils. In head imaging, such internal field inhomogeneities often occur around the petrous bone, leading to distortions in the temporal lobes, and also surrounding the sinuses, often leading to distortion around the anterior frontal regions. The magnetic field inhomogeneities cause pixels in the echo planar image to be shifted from where they should appear, and if the inhomogeneities are sufficiently bad, gross image distortion results. If the magnetic field inhomogeneities can be characterized by means of a residual field map throughout the volume of interest, then the distorted pixels can be relocated and intensity corrected to give a geometric distortion-free image. Accurate registration with high resolution anatomical images can then be made.

MRM 34:65–73 (1995)

From the Laboratory of Cardiac Energetics, NHLBI, National Institutes of Health, Bethesda, Maryland.

Address correspondence to: Peter Jezzard, Ph.D., Laboratory of Cardiac Energetics, Building 10 Room B1D161, National Institutes of Health, Bethesda, MD 20892.

Received December 15, 1994; revised March 10, 1995; accepted March 21, 1995.

0740-3194/95 $3.00

THEORY

The phase evolution of a pixel in a magnetic resonance image is dictated by the local magnetic field that it experiences. In general, for an elemental point in a volume of interest, the signal induced in the NMR receiver coil is given by

$$\partial S(x, y, z, t) \propto \rho(x, y, z)\exp\left[i2\pi\gamma\int_0^t B_0(x, y, z)dt\right] \cdot \exp[-t/T_2^{(*)}] \quad [1]$$

where the time origin is the excitation pulse, γ is the gyromagnetic ratio in Hz/Tesla, and $\rho(x,y,z)$ is the local spin density. In the absence of applied gradients and in a perfectly shimmed volume, the first exponential term in Eq. [1] reduces to unity in the rotating frame, and a simple exponential (free induction) decay of the signal results. In the case of a slice-selected imaging experiment in which phase encode (G_p) and read (G_r) gradients are applied, and with a field inhomogeneity term characterized by $\Delta B_0(x, y, z)$, the first exponential term in Eq. [1] becomes

$$\exp\left\{i2\pi\gamma\left[\int_0^t G_r(t)x\,dt + \int_0^t G_p(t)y\,dt + \int_0^t \Delta B_0(x, y, z)dt\right]\right\} \quad [2]$$

if we arbitrarily define x to be the read direction and y to be the phase encode direction. Thus, the field gradient history and field inhomogeneity determine the phase of the detected signal, and the phase evolution between subsequent digitizations of the phase determines the position of the pixel in the image. A convenient formalism for analyzing such experiments is the k-space notation (7, 8), in which the gradient history is characterized by making the substitution $k(t) = 2\pi\gamma\int G(t)dt$. The imaging experiment then becomes a matter of sampling k-space in the optimal way for the desired image information. For a conventional spin-warp or similar experiment, a line of k-space is collected for each excitation of the sample. In

the read and phase encode directions, this gives a phase evolution between adjacent points in k-space for the elemental pixel of

$$\Delta\phi_r = 2\pi\gamma[G_r x \mathrm{DW} + \Delta B_0(x, y, z)\mathrm{DW}], \qquad \Delta\phi_{\mathrm{pe}} = 2\pi\gamma\Delta G_{\mathrm{pe}} y \tau_{\mathrm{pe}} \quad [3]$$

where DW is the dwell time, ΔG_{pe} is the phase encoding step, and τ_{pe} is its duration.

It is evident from Eq. [3] that the phase evolution in the read direction of k-space is sensitive to the presence of magnetic field inhomogeneities, which would lead to a shift in the assigned position of the element in the Fourier transformed image of $N.\Delta B_0(x, y, z)/G_r$ field-of-view (FOV) pixels for an $N \times N$ matrix image of FOV. Under typical spin warp imaging conditions in the human head at 1.5 Tesla, this would correspond to an RMS pixel shift of approximately 1/10 pixel (assuming a field inhomogeneity of $\gamma < \Delta B_0(x, y, z) > = 12$ Hz, a 256 × 256 matrix size, and a sweep width of γG_rFOV = 32 kHz), which is barely noticeable in the image. In the phase encode direction, the pixel shift is theoretically zero, because no field inhomogeneity term contributes.

In contrast, the phase evolution between adjacent points in k-space for the elemental volume in an EPI experiment with trapezoidal read gradient waveforms and triangular phase encode blips, in which the whole of k-space is sampled following a single excitation of the sample, is given by

$$\Delta\phi_r = 2\pi\gamma[G_r x \mathrm{DW} + \Delta B_0(x, y, z)\mathrm{DW}], \qquad \Delta\phi_{\mathrm{pe}} = 2\pi\gamma[G_{\mathrm{pe}} y \tau_{\mathrm{ramp}} + \Delta B_0(x, y, z)(2\tau_{\mathrm{ramp}} + N.\mathrm{DW})] \quad [4]$$

in which τ_{ramp} is the ramp time of the switched gradients (see also the discussion by Farzeneh *et al.* (9)). First, it is evident from Eq. [4] that both the read and phase encode pixel positions are affected by the field inhomogeneity term, and secondly that the effects in the phase encoding direction are quite significant. Taking typical EPI parameters of a sweep width of 125 kHz, a gradient ramp time of 200 μs, and a 64 × 64 pixel matrix, one obtains an RMS pixel shift of 0.006 pixels in the read direction, and a pixel shift in the phase encode direction, which is bigger by a factor of $(2\tau_{\mathrm{ramp}} + N.\mathrm{DW})/\mathrm{DW}$. For the example parameters given here, this yields a phase encode RMS pixel shift of 0.7 pixels. Clearly, in some parts of the image, the pixel shift will be much larger than this, and gross distortion of the image will result. It is important to note, however, that the image distortion consists almost entirely of pixel shifts in the phase encode direction, with shifts in the read direction being negligible. Thus, a geometric distortion correction strategy need only consider shifts in the phase encode direction, and the problem reduces to solving for a set of linear 1-dimensional (1D) unwarps. Examples of the kinds of geometric distortion that can result from various applied field inhomogeneities are shown in Fig. 1, which illustrates echo planar images collected under a variety of shim conditions. (Note that the physical vertical direction, indicated by the presence of an air bubble in the phantom data, has been rotated to the horizontal in order that a consistent axis for the phase encode direction is maintained with the later figures.)

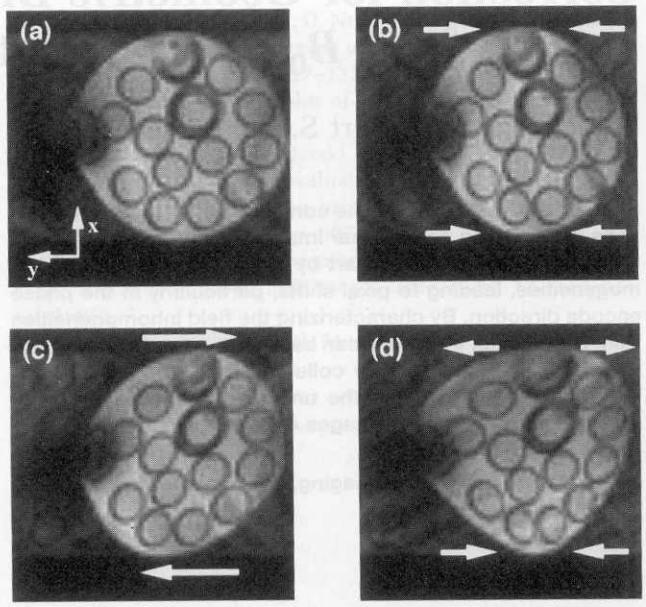

FIG. 1. Examples of snapshot gradient-recalled-echo EPI collected in the presence of a variety of shim conditions. In all images, the read direction (magnet x) is vertical and the phase encode direction (magnet y) is horizontal. (a) shows an image collected under well-shimmed conditions, demonstrating minimal geometric distortion. (b) shows the effect of a mis-set y shim, resulting in a contraction or expansion in the phase encode direction, depending on the sign of the shim mis-setting. (c) shows a mis-set x shim, which results in an apparent shearing of the image in the phase encode direction. (d) is the result of a mis-set $(x^2 - y^2)$ shim, resulting in a more complex geometric distortion. For all images, the acquisition parameters were as follows: 64 × 64 pixel resolution, 125-kHz bandwidth, 120-mm FOV, 4-mm slice thickness, 250 μs gradient ramp time, TE = 36 ms.

METHOD

To calculate the 1D pixel shifts, a field map is collected as part of the imaging experiment (10). This is accomplished by collecting a double-echo gradient recalled echo image, with the same FOV as the subsequent EPI data, but often at a higher resolution (a double echo sequence is used to eliminate B_1 phase errors, because these will be constant for the two echoes and will cancel in the phase subtraction). In fact, because a high resolution gradient echo image is often collected for use as an anatomical image as part of the imaging protocol, the alteration to a double-echo experiment need add no extra time to the total duration of the experiment. Once the phase map from each of the gradient echo images has been calculated and the π bounce points have been unwrapped, the field inhomogeneity map may be calculated according to $\Delta B_0(x, y, z) = (2\pi\gamma\Delta TE)^{-1}\Delta\phi(x, y, z)$. Care should be taken to avoid chemical shift artifacts in the field map due to the fat resonance either by use of a fat suppression pulse in the sequence, or by selecting an echo time difference such that the chemical shift contri-

bution has the same phase in each image, i.e., $\Delta TE = n.\Delta\nu_{fat}^{-1}$. Additionally, we have found it beneficial to smooth the images slightly before the phase map is calculated to provide for a smooth transition between distinct image regions such as the interhemispheric gap in coronal or axial sections. This amounts to convolving the image data set with typically a Gaussian kernel of width 3×3 pixels in a 256×256 pixel matrix.

Figure 2a shows an example of an unwrapped field map from a 9-cm diameter phantom that was imaged using a 2 Tesla animal imaging magnet attached to a GE/Bruker Omega spectrometer. In this case, the $(x^2 - y^2)$ shim was purposely mis-set, which is evident in the unwrapped field map. Figure 2b shows a gradient recalled echo planar image of the phantom acquired using the parameters given in the example above. Severe geometric distortion is apparent in the 64×64 pixel echo planar image, as opposed to a high resolution FLASH image acquired under the same shim conditions shown in Fig. 2c.

A 2D polynomial surface is then fitted to the field map to allow for some degree of extrapolation outside the region where the field inhomogeneity can be measured. This is done to account for regions that may contribute signal intensity, but which are not included in the unwrapped field map, either because they fall below the noise threshold set by the unwrapping algorithm or because they lie in a distinct region of the image, into which the phase unwrapping algorithm does not enter (it would be possible to unwrap distinct regions within the image, but an estimate would then need to be made to obtain the absolute phase shift between the regions - in the case of closely spaced regions or for a slowly varying field inhomogeneity, this would be feasible). A third order 2D polynomial fit is used to accomplish this, and, if desired, the fitted field map can then be replaced by the actual field map in those pixels where it is known. One caveat to the fitting procedure in cases where the field map data set is of a higher resolution and shorter echo time than a distorted gradient-echo EPI data set is that rapid field variations measured in the field map can lead to signal dropout in the EPI image rather than signal relocation. This condition occurs when the field gradient calculated from the field map causes a phase shift across the EPI pixel that approaches or exceeds 2π. The field map fit may be weighted against regions of the measured field map where this situation arises. An example of this effect is evident in the phantom data in Fig. 2 where signal around the air bubble yields a measurable field gradient in the field map, but leads to signal loss in the EPI data.

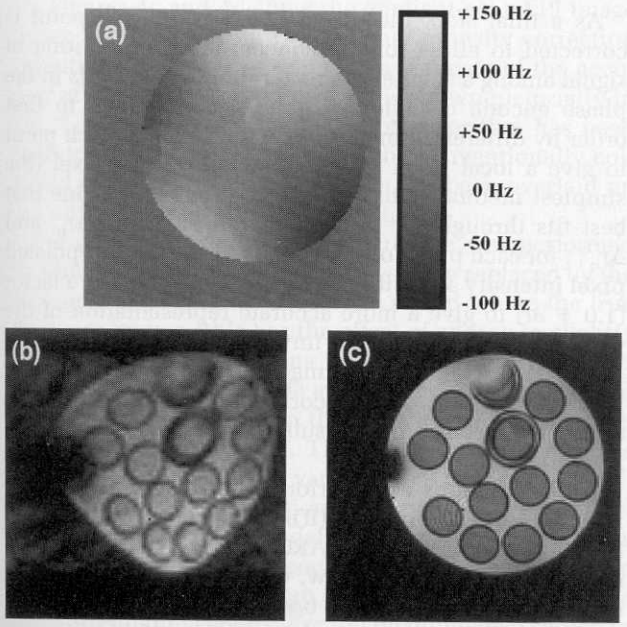

FIG. 2. (a) Unwrapped field map from the phantom shown in Fig. 1 under conditions of a mis-set $(x^2 - y^2)$ shim channel. (b) Echo planar image collected under the field inhomogeneity conditions shown in (a). (c) shows the corresponding conventionally collected gradient-echo image (TR = 500 ms, TE = 7 ms) acquired under the same shimming conditions.

One problem that can be encountered is "over fitting" of the field map outside the region where the field is known. This can lead to large deviations in the fitted field map, particularly at the edges of the data set. Figure 3 illustrates this problem for the same phantom shown in Fig. 2, in which the phase-unwrapped measured field inhomogeneity is shown in Fig. 3a, and the polynomial fitted surface is shown in Fig. 3b. The fit to the known field inhomogeneity in the sample is good, as shown in Fig. 3d (with an RMS deviation of 2.7 Hz over the measured region, corresponding to 0.17 pixels in the phase encode direction—this compares with an original RMS field variation of 31 Hz). However, toward the edges of the data set, outside the measured region, unrealistically large deviations in the fitted field map can result. If included in the eventual unwarping calculation, these large deviations will be interpreted as large pixel shifts at these points, and can result in unwarped signal intensity being "aliased" back to those pixels, where in fact no signal intensity should exist.

A method for dealing with this problem is to create a signal intensity mask from the high resolution image, and constrain the fitted field map to approach zero outside the sample. In this study, this has been accomplished using a two-step process. First, a dilation-structuring element (11) is used to expand the signal intensity mask from the unwrapping procedure slightly to avoid corrupting the fit in the region of the sample. We use a dilation structuring element consisting of a disk of radius P pixels, which is convolved with the binary signal intensity mask, and has the effect of expanding the mask and of filling in any small random regions which lie inside the actual sample, but which do not appear in the signal intensity mask because they have low signal-to-noise ratio in the phase map data. The value of P is chosen to be the smoothness value which is used in the subsequent smoothing operation, in which the expanded signal intensity mask is boxcar averaged to provide a gradual transition to zero outside the sample area. In this way, a mask that is unity throughout the sample, and falls to zero smoothly outside the sample, is created. The second step is to then multiply the dilated and smoothed signal intensity mask by the fitted field map to create the final field map estimate. An example of the result of this

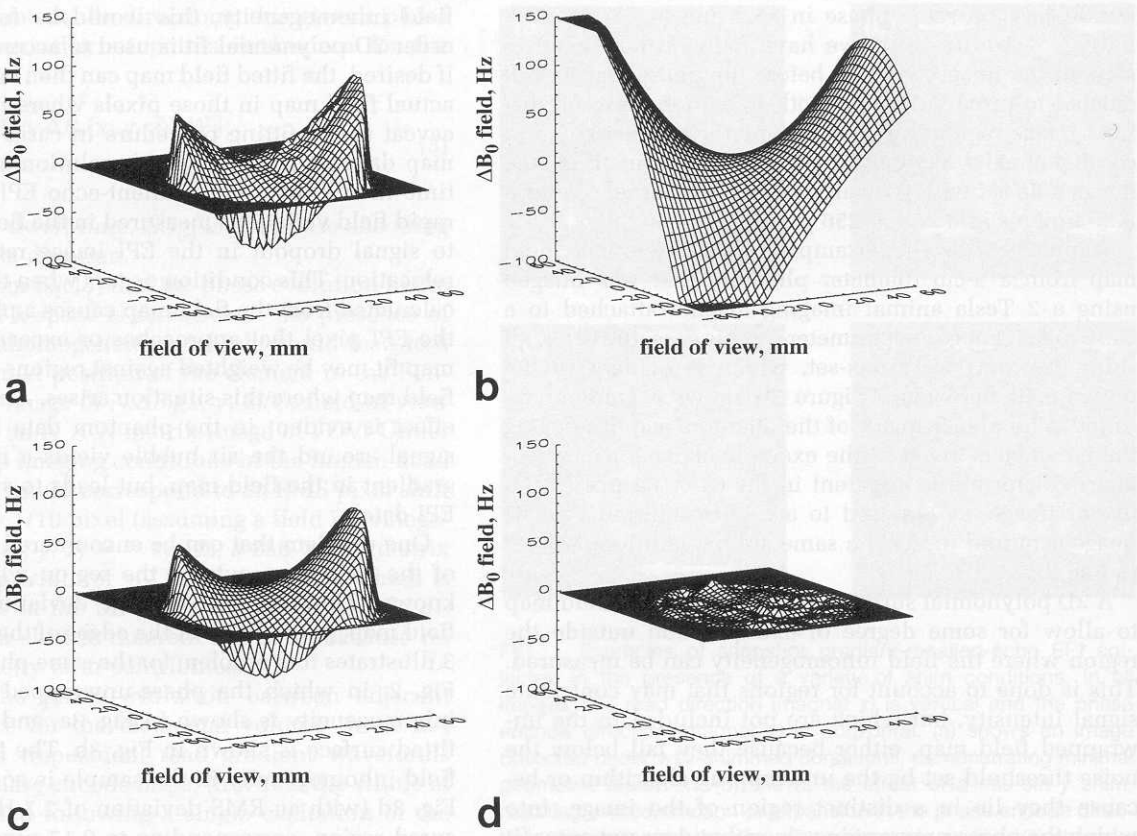

FIG. 3. (a) Stack plot of the measured field inhomogeneity in the phantom shown in units of Hz. A 2D surface is fitted to the field map as shown in (b). To avoid gross excursions in the fitted field map outside the region of the sample, the field map is constrained to fall smoothly to zero outside the sample, as shown in (c). (d) shows the residual field inhomogeneity map from actual and fitted data in the area where the field is known.

operation is shown in Fig. 3c, in which the field map shown in Fig. 3b has been multiplied by a dilated and smoothed signal intensity mask, in this case using a value of $P = 0.05 \times N = 3$ (for the data matrix size used here, $P = 3$ is the smallest pixel value that gives a disk dilation element).

The final field map is then converted into a pixel shift map according to the equation:

$$\Delta r_{\mathrm{pe}} = \gamma \Delta B_0(x, y, z).N(2\tau_{\mathrm{ramp}} + N.\mathrm{DW}). \quad [5]$$

Equation [5] is simply a mathematical way of saying that the phase encode shift, in units of pixels, is equal to the measured field inhomogeneity, converted to Hz, and divided by the effective spectral width per pixel. The location of a pixel in the geometrically distorted (warped) image is then related to the position of the pixel in the unwarped image by the formula

$$y^{w}_{pe} = y^{uw}_{pe} + \Delta r_{pe}(y^{uw}_{pe}), \quad [6]$$

where again the y direction has arbitrarily been taken to be the phase encode direction, and geometric distortion in the read direction has been ignored. For each phase encoding line in the echo planar image, a linear interpolation of the signal intensity in the warped image at pixel location $y^{w}_{pe} - \Delta r_{pe}(y^{uw}_{pe})$ is made and the interpolated intensity is placed at position y^{uw}_{pe}. Alternatively, a decomposed first order phase correction could be applied in the Fourier domain (12).

As a final step, the image intensity at each point is corrected to allow for the concentration or dilution of signal among a smaller or greater number of pixels in the phase encode direction. This is accomplished to first order by differentiating the pixel shift map at each point to give a local pixel shift gradient of ∂r per pixel (the simplest method is to take the gradient of the line that best fits through the pixel shift values Δr_{n-1}, Δr_n, and Δr_{n+1} for each pixel location n). The linearly interpolated pixel intensity at position n is then multiplied by a factor $(1.0 + \partial r)$ to give a more accurate representation of the pixel intensity value in the unwarped image. It should be noted, however, that the image noise is no longer uniform when this type of correction is used, and this should be borne in mind if subsequent statistical analysis is attempted.

All calculations were performed using code written in interactive data language (IDL, Research Systems, Inc., Boulder, CO) on a Sun SPARC 10 workstation (Sun Microsystems, Mountain View, CA). A user friendly front end for the code allows the user to correctly co-orient the EPI and field map data, and the pixel shift map is then calculated and saved.[1] The pixel shift map can be applied to each of the image time points from a subsequent

[1] This software is freely available to interested individuals from P.J. Please note, however, that a license is required to run under the IDL platform.

EPI data run, resulting in a set of unwarped images from a time series. Alternatively, if desired, image processing operations (such as blood volume calculations, etc.), can be performed on the warped EPI time series, and then the resulting functional map can be unwarped for registration purposes. The calculation of the pixel shift map for a 128 × 128 pixel field map is completed in approximately 10 s, and the unwarping procedure itself is a computationally fast step (<1 s).

For the human studies, a 1.5 Tesla GE Signa scanner was used (GE Medical Systems, Milwaukee, WI), with a specially designed *z*-axis local gradient coil (13), which is used to provide fast gradient switching in the read direction. The EPI parameters used were: 64 × 64 pixels, 200 mm FOV, 180 μs gradient ramp times in the read direction, 125 kHz sweep width, and a 5-mm slice thickness. A gradient echo EPI sequence was used with an echo time of 40 ms. Additional human data were acquired at 4 Tesla, using a whole body 4 T magnet (Oxford Magnet Technology, UK), linked to a GE/Bruker Omega spectrometer (Bruker, Fremont, CA). An identical *z*-axis local gradient coil was used on the 4 Tesla system, and identical EPI acquisition parameters, except for a shorter echo time of TE = 28 ms.

RESULTS

Initial phantom results were obtained from the 2 Tesla animal system, and are summarized in Fig. 4. A conventional FLASH image of the phantom, which consisted of a 9-cm diameter bottle filled with $CuSO_4$-doped water, which in turn contained a number of smaller water-filled tubes, is shown in Fig. 4a. The calculated pixel shift map used to unwarp the echo planar images is shown in Fig. 4b. Figures 4c and 4d show the gradient-echo EPI image before and after the unwarping and intensity correction algorithm has been performed. An estimate of the accuracy of the re-registration process is shown pictorially in Fig. 5, in which an edge detection algorithm has been used to highlight the features in the conventionally collected image, and this information has been overlaid on the unwarped and warped EPI data sets.

For comparison, a second calculation was performed in which the fitted field map values were replaced by the measured field map values in the region where the true field was known (this has the effect of adding in slightly more small scale variations in the pixel shift map). No noticeable alteration in the appearance of the unwarped image was evident, and in this case it seemed that both methods were equivalent. This is likely because of the origin of the residual field variations, as discussed below, and because of the resolution difference between the EPI data and the phase map data. In practical situations, a map of the residuals should provide a guide as to whether the fitted field map accurately characterizes the true field inhomogeneity. For the phantom data shown in Fig. 5, the field variations observed in the residuals map correspond to the signal voids at the locations of the plastic tops and walls of the smaller tubes. In our experience, much of the residual field inhomogeneities are artifactual, and so the fitted field map should be used when possible (this also minimizes any signal-to-noise

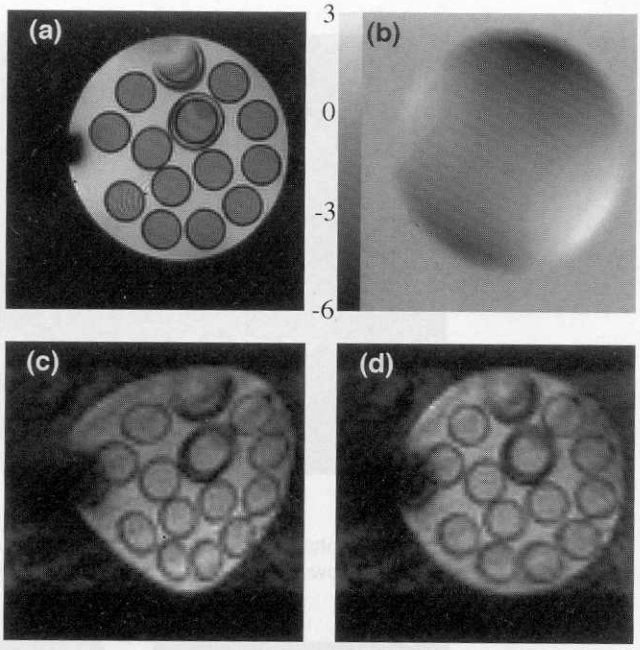

FIG. 4. (a) shows the first image from a double gradient-recalled-echo image data set used to calculate the field inhomogeneity map, and (b) shows the calculated field inhomogeneity map used to correct the echo planar data, with a pixel shift scale shown in units of pixels. (c) and (d) show the original and unwarped echo planar data, respectively.

reduction caused by noise in the field map calculation process).

Experiments conducted to identify the origin of the residual high spatial frequency phase shifts in the brain reveal that flow effects contribute substantially, causing phase shifts unrelated to the magnetic field inhomogeneity. When flow compensation was implemented, the structural information evident in the residuals map reduced. Figure 6 shows this in the case of two phase map studies performed at 4 Tesla. Figures 6b and 6c show the residuals map (measured field minus fitted field) obtained without and with flow compensation, respectively. The blood vessel features evident in Fig. 6b are not evident in Fig. 6c. When the study was repeated at a lower resolution of 64 × 64 pixels (Fig. 6e and 6f), again the anatomically derived phase discontinuities decreased with flow compensation. The remaining field dip evident in the center of Figs. 6c and 6f is relatively small (<5 Hz) and makes minimal difference to the unwarping process when included. Indeed, the phase noise in maps such as Figs. 6c and 6f makes the appearance of the unwarped EPI image inferior when the measured field information is used for distortion correction rather than the fitted field information. Around the orbit and petrous bone, very strong field gradients were evident in the field map data for slices that cut through these areas, which were still evident in residuals maps. However, these strong gradients lead to signal drop out in the echo planar image rather than signal relocation, and so these deviations from the fitted field map are unimportant.

Two examples of the use of the algorithm in practical situations are shown in Figs. 7 and 8, in which a normal

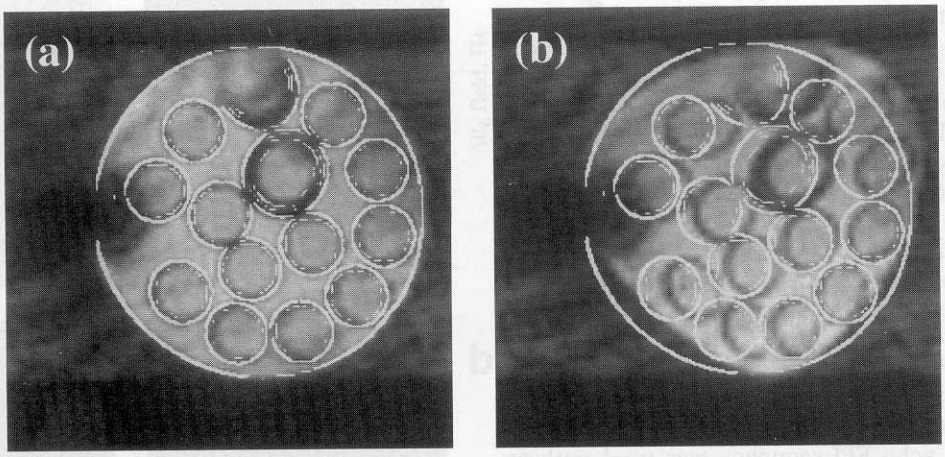

FIG. 5. Overlay of the edge-enhanced high resolution structural information onto the echo planar data. (a) shows an overlay onto the corrected EPI data, and (b) shows an overlay onto the uncorrected EPI data.

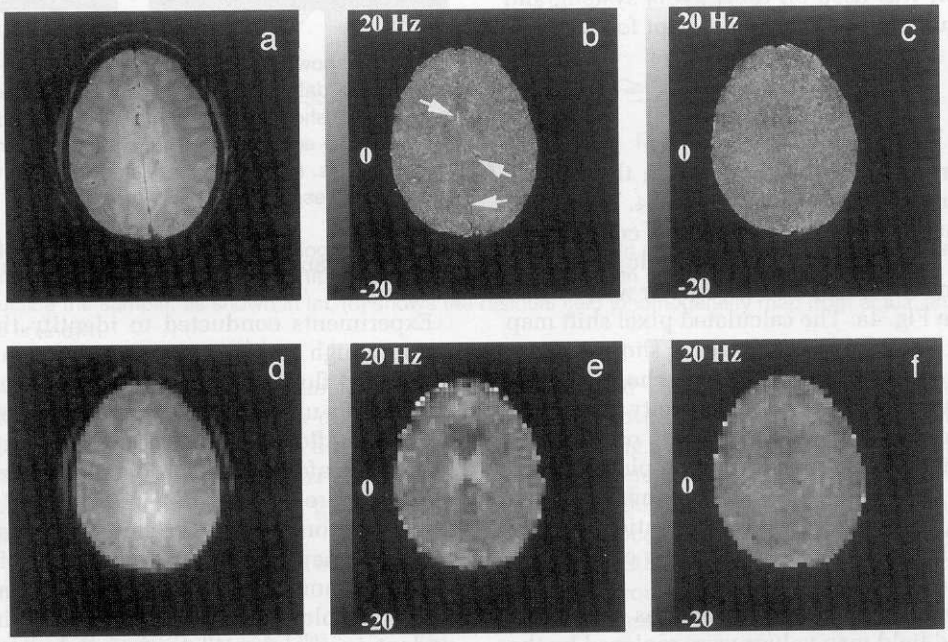

FIG. 6. (a) 256 × 256 pixel resolution GRASS scan obtained at 4 Tesla, showing an axial slice through the head of a normal volunteer. (b) shows the magnetic field residuals map (measured field inhomogeneity minus fitted field inhomogeneity) in units of Hz when no flow compensation was used. Some anatomically derived features are evident in the residuals map, indicated by arrows. (c) shows the residuals map when flow compensation was used. (d)-(f) show similar data for a lower resolution data set of 64 × 64 pixels. Again the anatomically derived structure in the phase maps is reduced with flow compensation.

male subject was imaged using a surface coil to receive at a field strength of 1.5 Tesla. The standard shim settings were used to collect the structural and EPI data in both sagittal (Fig. 7) and coronal (Fig. 8) sections. For the sagittal data, an RMS field inhomogeneity variation of 29.7 Hz was measured, with typical deviations in the inferior temporal region of 40 to 50 Hz, and deviations of −50 to −100 Hz being recorded in the inferior frontal region. In the coronal data set, similar field inhomogeneities of around 45 Hz were recorded in the inferior temporal lobe and brain stem. The residuals map between the measured and fitted field map showed an RMS field variation of 5 Hz in the sagittal data set (mostly evenly distributed throughout the slice, except near the most inferior part of the frontal lobe) and 4 Hz in the coronal data set (evenly distributed throughout the slice). In Fig. 7c, which shows the simple sagittal echo planar image, geometric distortion is particularly evident in the temporal lobe, in which field inhomogeneities in the region of the petrous bone cause an anterior shift in pixel position. Additional distortion is evident in the cerebellum, which has been artifactually expanded in the anterior-posterior

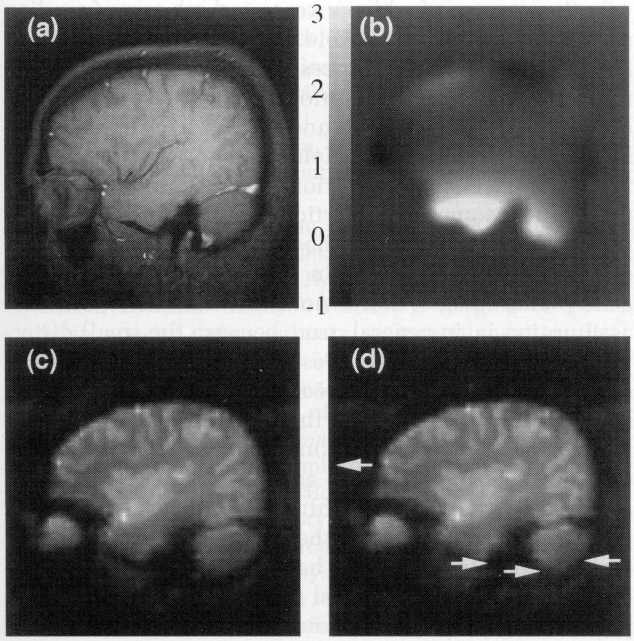

FIG. 7. (a) shows the first image from a double-echo sagittal FLASH image data set used to calculate the field inhomogeneity map. A 1.5 Tesla field strength, a 200-mm FOV, and a slice thickness of 5 mm were used. (b) shows the calculated field inhomogeneity map used to correct the echo planar data, which had a maximum positive field deviation of 50 Hz and a maximum negative field deviation of −100 Hz. (c) and (d) show the original and unwarped echo planar data, respectively. The following EPI parameters were used: 64 × 64 pixels, 200-mm FOV, TE = 40 ms, 125-kHz sweep width, 180-μs gradient ramp time, 5-mm slice thickness. The arrows indicate the directions of the pixel shifts calculated from the field shift.

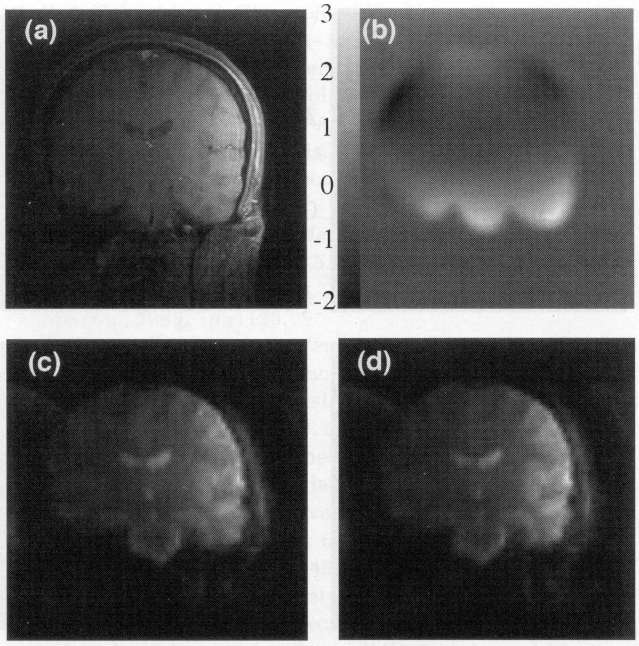

FIG. 8. (a) shows the first image from a double-echo coronal FLASH image data set used to calculate the field inhomogeneity map. A 1.5 Tesla field strength, a 200-mm FOV, and a slice thickness of 5 mm were used. (b) shows the calculated field inhomogeneity map used to correct the echo planar data. (c) and (d) show the original and unwarped echo planar data, respectively. The same imaging parameters as in Fig. 7 were used for the echo planar images.

direction, and is also present elsewhere in the image, but is more difficult to see by eye. Figure 7d shows the undistorted, unwarped echo planar image obtained using the field map fit shown in Fig. 7b. Figures 8c and 8d show the uncorrected and corrected echo planar scans obtained in the coronal plane.

At higher than 1.5 Tesla field strengths, the susceptibility effects are proportionately enhanced, and so a method for correction of geometric distortion in EPI data is even more desirable. Figure 9 shows structural and echo planar human data obtained using a surface coil at 4 Tesla. Similar EPI acquisition parameters as described above, other than a slightly shorter echo time of 28 ms, which have previously been used for high field functional imaging (14) were used at 4 Tesla. At 4 Tesla, we have found it desirable to individually shim each volunteer before attempting EPI, using an analytical algorithm that optimizes currents up to the third order (15). Even so, field inhomogeneities tend to remain, as are evident in Fig. 9b. In the case of this sagittal section, taken 35 mm left of midline, an RMS field variation of 26 Hz was recorded throughout the brain region, with a maximum deviation of 100 Hz in the temporal lobe and cerebellum, and a minimum deviation of −40 Hz in the frontal lobe. The uncorrected and corrected echo planar images are shown in Figs. 9c and 9d. Note that the eye position remains distorted because it falls outside the region of the fitted field map. Additionally, evidence of greater signal loss in the temporal lobe is seen in the 4 Tesla image when compared with the 1.5 Tesla image because of the larger magnitude of the susceptibility gradients there.

DISCUSSION

For the technique outlined above to work well, details of the acquisition parameters and reconstruction algorithm used should be accounted for. On many scanners that have echo planar capabilities, a simple EPI MBEST sequence is used in which the spectrometer digitizer timing is adjusted such that minimal ghosting results from a simple Fourier transformation of the k-space data. When this is the case, the algorithm as presented above will require no modification. Problems may arise, however, if eddy currents are induced in the magnet during the echo planar sequence that are different from those induced during the field mapping sequence, in which case the effective field inhomogeneity for the EPI sequence could be different from that measured using the double-echo gradient echo sequence, and may even be time varying. For the equipment used in these studies, eddy currents were not found to be significant. Similar problems may occur if certain gradient "tweakers" are used in the EPI sequence, which are not accounted for in the geometric correction. In particular, some groups use a read gradient adjuster (used to force the echoes to have a constant separation throughout the echo train) which is added on

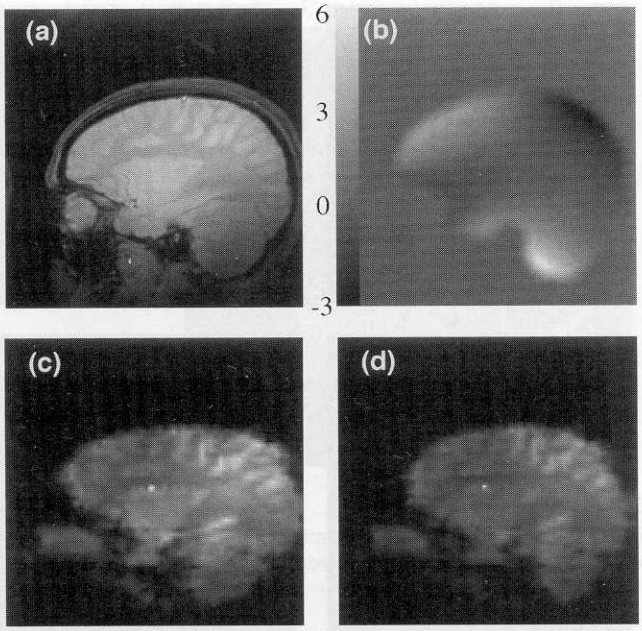

FIG. 9. (a) shows the first para-sagittal image from a double-echo sagittal GRASS image data set used to calculate the field inhomogeneity map. A 4 Tesla field strength, a 200-mm FOV, and a slice thickness of 5 mm were used. (b) shows the calculated field inhomogeneity map used to correct the echo planar data, which had a maximum positive field deviation of 100 Hz and a maximum negative field deviation of −40 Hz. (c) and (d) show the original and unwarped echo planar data, respectively. The same imaging parameters as in Fig. 7 were used for the echo planar images, except for a lower *TE* value of 28 ms.

to the oscillating read gradient, and has the effect of simulating a shim correction in the read direction. In such cases, the effective shim correction caused by the gradient "tweaker" should be calculated and added on to the measured field map.

Further problems can arise if a phase correction algorithm is used to correct for Nyquist ghosts caused by timing differences in the sampling of even and odd echoes. When a strategy is used in which a single phase correction is applied to all even echoes and a single phase correction is applied to all odd echoes (16), no modification of the geometric distortion algorithm is required. However, if a more sophisticated phase correction scheme is used, then the field map may not represent the required pixel shifts. Such a case is when a separate phase correction is applied to each line in *k*-space (calculated from a reference scan in which no phase encode gradient is used). In general, this will cause a phase roll in the phase encode direction that often partially corrects for field inhomogeneities in the sample. In practice, this often amounts to a linear phase roll in the phase encode direction, which substitutes for the read gradient "tweaker" described above. Thus, a first order fit to this phase roll, as obtained from the phase corrections used in the reconstruction algorithm, can often be used to successfully correct the pixel shift map according to the relation $\Delta r = \partial\phi/\partial N.(N/2\pi)$, where $\partial\phi/\partial N$ is the linear phase roll fit and N is the number of pixels in the phase encode direction.

In the absence of eddy currents and other confounding sources of artifact in the field map calculation, the accuracy of the unwarping process can be assessed from the residuals map, the assumptions being that the high resolution anatomical map is undistorted by the field inhomogeneities, and that the field inhomogeneities account for all the geometric distortion in the echo planar image (note that geometric distortion resulting from gradient nonlinearities inherent in the gradient coil design would still be present and equal in both the conventional and echo planar images, and is not dealt with here). The first assumption is, in general, true, because the small distortions caused to the high resolution image in the read direction are sub-pixel in scale, where the pixel dimension would typically be on the order of 1 mm in dimension. The second assumption should be true when gradient waveform fidelity is good (i.e., the gradient coil amplifiers are driven within their linear range), and when chemical shift and other artifacts described above are absent. Our experience has been that the unwarping algorithm results in a spatial unwarping that is also subpixel in accuracy, because our field map residuals show an RMS accuracy of approximately 5 Hz (or 0.25 pixels in the EPI phase encoding direction). With EPI pixel sizes of 2 to 3 mm, and temporal lobe and anterior frontal lobe field map residuals of 10 Hz or 0.5 pixels, re-registration accuracies ~1 to 1.5 mm are typical in those regions, with re-registration accuracies ~0.5 to 1 mm elsewhere. The accuracy of re-registration tends to increase with lower field strengths, because the inherent susceptibility-induced field gradients are proportionately lower in magnitude.

In summary, if a pixel shift map can be constructed that accurately reflects the field inhomogeneities present in the sample, and details of the acquisition parameters and image reconstruction algorithm that may affect this estimate can be accounted for, then the algorithm described in this paper has been found to provide a robust method for the correction of geometric distortion in echo planar images, and does not exhibit the same sensitivity to low signal to noise or ghosting that alternative geometric distortion correction algorithms do (17). The technique has been demonstrated in phantom studies and in human subjects, and has considerably aided the task of making comparisons between anatomical information in high resolution structural images and functional information in lower resolution functional images.

ACKNOWLEDGMENTS

The authors thank the *In Vivo* NMR Center at the National Institutes of Health, where part of this work was conducted; A. Scott Chesnick for excellent technical assistance; Dr. Han Wen for providing a phase unwrapping algorithm; and Dr. Eric Wong for providing the EPI code for the 1.5 Tesla system.

REFERENCES

1. P. Mansfield, Multi-planar image formation using NMR spin echoes. *J. Phys. C* **10,** L55-L58 (1977).

2. P. Mansfield, I. L. Pykett, Biological and medical imaging by R. NMR. *J. Magn. Reson.* **29,** 355–373 (1978).
3. R. R. Rzedzian, I. L Pykett, Instant images of the human heart using a new whole body MR imaging system. *Am. J. Roentgenol.* **149,** 245–250 (1987).
4. B. R. Rosen, J. W. Belliveau, J. M. Vevea, T. J. Brady, Perfusion imaging with NMR contrast agents. *Magn. Reson. Med.* **14,** 249–265 (1990).
5. K. K. Kwong, J. W. Belliveau, D. A. Chesler, I. E. Goldberg, R. M. Weisskoff, B. P. Poncelet, D. N. Kennedy, B. E. Hoppel, M. S. Cohen, R. Turner, H.-M. Cheng, T. J. Brady, B. R. Rosen, Dynamic magnetic resonance imaging of human brain activity during primary sensory stimulation. *Proc. Natl. Acad. Sci. (USA)* **89,** 5675–5679 (1992).
6. P. A. Bandettini, E. C. Wong, R. S. Hinks, R. S., Tikofsky, J. S. Hyde, Time course EPI of human brain function during task activation. *Magn. Reson. Med.* **25,** 390–397 (1992).
7. S. Ljunggren, A simple graphical representation of Fourier-based imaging methods. *J. Magn. Reson.* **54,** 338–343 (1983).
8. D. B. Twieg, The k-trajectory formulation of the NMR imaging process with applications in analysis and synthesis of imaging methods. *Med. Phys.* **10,** 610–621 (1983).
9. F. Farzaneh, S. J. Riederer, N. Pelc, Analysis of T_2 limitations and off-resonance effects on spatial resolution and artifacts in echo-planar imaging. *Magn. Reson. Med.* **14,** 123–139 (1990).
10. E. A. Schneider, G. Glover, Rapid in vivo proton shimming. *Magn. Reson. Med.* **18,** 335–347 (1991).
11. R. M. Haralick, S. R. Sternberg, X. H. Zhuang, Image analysis using mathematical morphology. *IEEE Trans. Pattern Analysis Machine Intelligence* **PAMI-9,** 532–550 (1987).
12. R. M. Weisskoff, T. L. Davis, Correcting gross distortion on echo planar images, *in* "Proc., SMRM, 11th Annual Meeting, Berlin, 1992," p. 4515.
13. R. Turner, R. Vavrek, J. Maier, D. LeBihan, EPI diffusion imaging of the brain at 1.5 tesla without motion artifact using a head gradient coil, *in* "Proc., SMRM, 8th Annual Meeting, 1989," p. 1123.
14. R. Turner, P. Jezzard, H. Wen, K. K. Kwong, D. LeBihan, T. Zeffiro, R. S. Balaban, Functional mapping of the human visual cortex at 4 and 1.5 tesla using deoxygenation contrast EPI. *Magn. Reson. Med.* **29,** 277–279 (1993).
15. H. Wen, "High Field Magnetic Resonance Imaging," Ph.D. Thesis, University of Maryland, 1994.
16. E. C. Wong, Shim insensitive phase correction for EPI using a two echo reference scan, *in* "Proc., SMRM, 11th Annual Meeting, Berlin, 1992," p. 4514.
17. R. Bowtell, D. J. O. McIntyre, M.-J. Commandre, P. M. Glover, P. Mansfield, Correction of geometric distortion in echo planar images, *in* "Proc., SMR, 2nd Annual Meeting, San Francisco, 1994," p. 411.